GRP Simulations: Simple Boundaries, Complex Wave Phenomena

J. Falcovitz, M. Ben-Artzi
Institute of Mathematics, the Hebrew University of Jerusalem, Jerusalem 91904, Israel;
e-mail: ccjf@math.huji.ac.il

Abstract. Initial value problems for hyperbolic conservation laws are well known to produce complex wave structures even when the geometric setup is simple (e.g. 2-D wedge). The GRP scheme for compressible flow is therefore introduced (and validated) in the simpler context of scalar conservation laws. A good agreement between numerical and exact solutions for a case of complex 2-D (scalar) "shock interaction" supports the validity of the Strang-like operator splitting. An experimental flow visualization and the respective 2-D GRP computations for a case of second shock reflection from a double wedge show excellent agreement. The total force due to shock loading of a suspended model in a vertical shock tube is compared to accelerometer-measured history. A good agreement was obtained for a sphere. For a cone suspended by its apex, the square root of the drag force is theoretically a linear function of time, which is well replicated by the GRP solution. A disagreement with experimental data suggests that in this case the method needs further refinement.

1. Introduction

In this presentation we examine the GRP method for hyperbolic conservation laws (Ben-Artzi and Falcovitz, 2003) in test cases involving multidimensional shock interactions. We do so first in the (simpler) context of scalar conservation laws, then proceed to the fluid dynamical (Euler) equations by considering cases where experimental observations are available.

The interaction of shock waves with boundaries of various shapes is well known to result in complex wave structures even under simple geometric setups. A significant research effort has been devoted in the past half-century to the (experimental) observation and the (theoretical) understanding of the wave patterns produced by shock reflection from simple boundaries, such as wedges, cylinders or spheres. In fact, the Shock Wave Research Center of Tohoku University, under the leadership of Professor K. Takayama, has played a key role in the development of flow visualization methods and in applying them to studies of diverse phenomena involving complex shock wave interactions.

The theory of fluid dynamics and its underlying mathematical foundations of hyperbolic conservation laws have advanced significantly since the pioneering work of J. von Neumann (1943) on two-dimensional oblique shock reflection. With all that progress our understanding of shock interaction phenomena, even in the reduced case of two space dimensions, remains conspicuously incomplete.

The basic reason for that is the complexity inherent in constructing solutions to multidimensional initial value problems of systems of hyperbolic conservation laws. In the case of *one-dimensional* space our mathematical understanding is quite good. Here the "Riemann problem" (having an initial data of two uniform states separated by a point of discontinuity) is known to have a unique (entropy) solution. This self-similar solution is composed of three types of "elementary" waves, namely a shock wave (SW), a contact discontinuity, and a centered rarefaction wave (CRW). In the fluid dynamical case a Riemann problem is resolved by a fan of three waves consisting of a left-facing wave (SW or CRW), a right-facing wave (SW or CRW), and a contact discontinuity separating them. For other systems of hyperbolic conservation laws in one space dimension, the number of elementary waves resolving a Riemann problem is equal to the number of equations in that system.

Unfortunately, solutions to *multidimensional* Riemann problems (e.g., a data consisting of a uniform state in each of the four quadrants of the x, y plane) are genuinely multidimensional, and no set of simple "elementary" waves is known in this case. Shock interactions, as well as other initial value problems leading to discontinuous wave structures, can therefore be resolved only by means of numerical computation. It is interesting to observe in this regard that "Riemann schemes" for hyperbolic conservation laws (Godunov method being the first and GRP being a natural second-order extension) are generally based on solutions to (one-dimensional) Riemann problems at cell-interfaces. In other words, while a *finite-difference approximation* to multidimensional wave structures can be obtained by resorting to the set of one-dimensional "elementary" waves, the corresponding *exact solution* cannot be constructed by means of that set.

The GRP scheme will be briefly outlined in Section 2, followed by scalar conservation laws examples in Section 3. An elaborate case of fluid dynamical shock interaction in two space dimensions is given in Section 4, including comparison to experimental visualization. In Section 5 we consider accelerometric measurement of the drag force due to shock interaction with suspended sphere or cone, comparing measured and calculated force histories. Section 6 contains a summary and concluding remarks.

2. Outline of the GRP Scheme

The GRP scheme is based on solving a generalized Riemann problem (GRP) at each cell-interface of the computational grid. The data for this initial value problem is piecewise linear in cells and discontinuous at cell-interfaces, as shown schematically in Figure 1.

Loosely stated, the solution to a fluid dynamical GRP (for short time) is obtained as a modification of the (self-similar) wave structure resolving the "associated Riemann problem" (i.e., the Riemann problem having the same initial jump at the interface). More specifically, solving the GRP consists in first finding the velocity and pressure (u^*, p^*) at the contact discontinuity separating the two waves that resolve the associated Riemann problem, and second, finding the corresponding time derivatives $(\dot{u}^*, \dot{p}^*)$ which determine (to first-order accuracy) the non-self-similar evolution of these wave. It is well known that (u^*, p^*) are obtained from the intersection of a "left interaction curve" and a "right interaction curve"

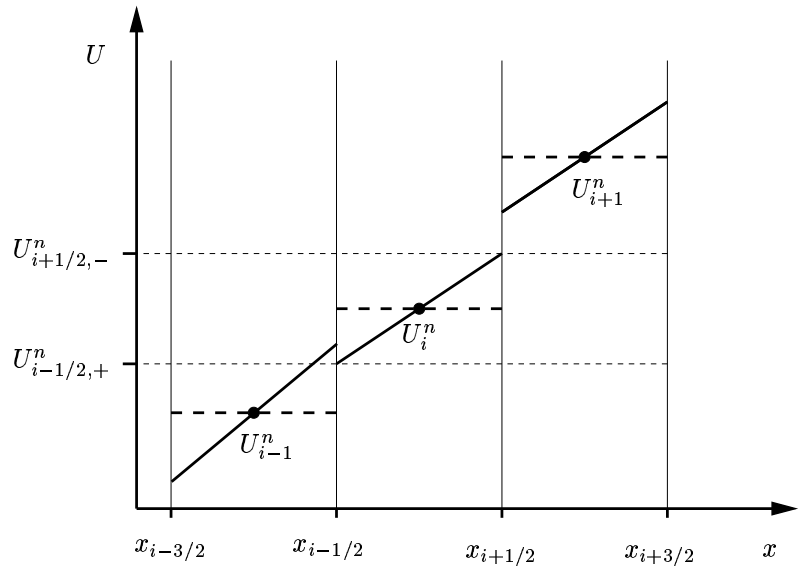

Figure 1. Piecewise linear distribution $U^n(x)$ of variable in cells.

in the (u,p) plane. Likewise, the time-derivatives $(\dot{u}^*, \dot{p}^*)$ are obtained from the intersection of two *linear* interaction curves on the $(\dot{u}, \dot{p})$ plane. The expressions for these linear curves are derived by a careful analysis of the wave structure resolving the GRP in the vicinity of the singular point $(x,t) = (0,0)$. We refer to Ben-Artzi and Falcovitz (2003), Chapter 5, for a detailed account of the fluid dynamical GRP analysis.

Here we introduce the GRP scheme in the simpler context of a scalar conservation law (*ibid*, Chapter 3), since the key ideas are analogous to those of a system of conservation laws. Consider the initial value problem for the scalar conservation law

$$\frac{\partial u}{\partial t} + \frac{\partial f(u)}{\partial x} = 0, \qquad t \geq 0, \tag{1}$$

where the function $u = u(x,t)$ is subject to the initial data

$$u(x,0) = u_0(x), \tag{2}$$

and where the flux function $f(u)$ is assumed to be convex, i.e., $f''(u) > 0$.

In a finite-difference one-step algorithm for (1)–(2) it is assumed that an initial profile $U^n(x)$ is given as an approximation to the solution $u(x,t^n)$ at time level t^n. The algorithm is designed to produce a new profile $U^{n+1}(x)$ at time level $t^{n+1} = t^n + \Delta t$ which is consistent with the differential equation (1). Briefly stated, the GRP finite-difference scheme for (1)–(2) is

$$U_i^{n+1} = U_i^n - \frac{\Delta t}{\Delta x}\Big(f_{i+1/2}^{n+1/2} - f_{i-1/2}^{n+1/2}\Big), \tag{3}$$

where, referring to the discretization scheme shown in Figure 1, U_i^n denotes the average value of $U^n(x)$ over cell i at time level t^n. The cell i is the interval (of length Δx) $x_{i-1/2} <$

$x < x_{i+1/2}$ bounded by the cell-interface points $x_{i\pm1/2}$, with $n+1/2$ denoting the midpoint of the time interval $t^n < t < t^{n+1}$. By $f_{i\pm1/2}^{n+1/2}$ we denote the "numerical flux" at the respective cell-interface point, averaged over the time-step.

Godunov (1959) proposed to take the approximating profile $U^n(x)$ as piecewise constant and to solve at each cell-interface $i+1/2$ a Riemann problem having the initial data $[U_i^n, U_{i+1}^n]$. The constant flux evaluated along the line $x = x_{i+1/2}$ is then taken as the numerical flux $f_{i+1/2}^{n+1/2}$ in (3).

For the GRP scheme, the approximating profile $U^n(x)$ is piecewise linear as in Figure 1. The fluxes $f_{i+1/2}^{n+1/2}$ are evaluated in terms of the variables $U_{i+1/2}^{n+1/2}$ at the midpoint of the time step. These are evaluated analytically by solving the generalized Riemann problem at the respective cell-interface as follows. First the initial (discontinuous) values at that interface are determined by the (known) cell gradients ("slopes") s_i^n according to

$$U_{i+1/2,\pm}^n = \begin{cases} U_{i+1}^n - \frac{\Delta x}{2} s_{i+1}^n, & "+", \\ U_i^n + \frac{\Delta x}{2} s_i^n, & "-" . \end{cases} \tag{4}$$

With these values the associated Riemann problem is solved (as in the Godunov case), giving rise to to the value $U_{i+1/2}^n$ (which is the instantaneous value of the variable following the resolution of the initial discontinuity at $x_{i+1/2}$). Finally, the time-derivative $\left(\frac{\partial U}{\partial t}\right)_{i+1/2}^n$ is evaluated. This step is really the cornerstone of the GRP algorithm. The time-derivative is evaluated analytically using Equation (1) and the given initial piecewise linear data. Observe that both $U_{i+1/2}^n$ and $\left(\frac{\partial U}{\partial t}\right)_{i+1/2}^n$ are determined in a way that takes into account the direction of the waves (characteristics) around the singularity. Naturally, in the case of the fluid dynamical system this procedure is more elaborate than in the case of a scalar conservation law, due to the complexity of the wave pattern emanating from the initial singularity.

The resulting scheme falls into the category of the so-called upwind schemes (in contrast to the Lax-Wendroff scheme which is second-order but "centered").

The time-centered flux for the second-order accurate GRP approximation is thus given by

$$f_{i+1/2}^{n+1/2} = f\Big(U_{i+1/2}^n + \frac{\Delta t}{2}\Big(\frac{\partial U}{\partial t}\Big)_{i+1/2}^n\Big). \tag{5}$$

The set of flux values $\left\{f_{i+1/2}^{n+1/2}\right\}$ are then used in the finite-difference approximation (3) for the new cell-average values.

Finally, the new slopes have to be evaluated. The GRP scheme calls for a kind of time integration for slopes. To that end we use the GRP solution, integrating the cell-interface values $U_{i+1/2}^n$ from t^n to t^{n+1} as follows

$$U_{i+1/2}^{n+1} = U_{i+1/2}^n + \Delta t\Big(\frac{\partial U}{\partial t}\Big)_{i+1/2}^n, \tag{6}$$

These values are used for the sole purpose of determining the new slopes, which are given by the centered-difference expression

$$s_i^{n+1} = \Big(U_{i+1/2}^{n+1} - U_{i-1/2}^{n+1}\Big)/\Delta x \tag{7}$$

As with all Riemann schemes of second-order accuracy, a monotonicity constraint (i.e., "slope limiter") is imposed on the new slopes by requiring that for every cell i (see Figure 1) the five-value sequence

$$\left[U_{i-1}^{n+1},\, U_{i-1/2,+}^{n+1} = U_i^{n+1} - s_i^{n+1}\Delta x/2\,,\, U_i^{n+1},\, U_{i+1/2,-}^{n+1} = U_i^{n+1} + s_i^{n+1}\Delta x/2\,,\, U_{i+1}^{n+1}\right] \quad (8)$$

be monotonic. If it is not so, the slope s_i^{n+1} is modified by "pivoting", i.e., reduced in absolute value by the minimal amount required to satisfy (8). It should be noted that at no time during this "followup" stage of the GRP algorithm do we modify the cell average values U_i^{n+1} which have been determined by the finite-difference relation (3).

3. Scalar Conservation Laws

Let us start with the one-dimensional scalar conservation law known as the Burgers equation which is given by (1) with flux function $f(u) = u^2/2$. Two shock wave test cases are considered for this equation. The first (Figure 2(a)) is with the step function data

$$u(x,0) = \begin{cases} 1 & x < 0.22\,, \\ 0 & x > 0.22\,; \end{cases} \quad (9)$$

the second (Figure 2(b)) has the "compressive" ramp function data

$$u(x,0) = \begin{cases} 1 & x < 0.22\,, \\ 1 - 2.5(x - 0.22) & 0.22 < x < 0.62\,, \\ 0 & x > 0.62\,. \end{cases} \quad (10)$$

The solution in the two cases is computed for times $t = 0.80$ and $t = 0.40$ respectively, where the exact solutions are identical – a unit step function localized at $x = 0.62$ (see Figures 2(a), 2(b)). The computation domain was the interval $0 < x < 1$ which was divided into 25 equal cells ($\Delta x = 0.04$). The time step was $\Delta t = 0.02$ (half the CFL limit). We remark that the points of discontinuity in the initial data and in the exact solution at the final time ($t = 0.80$ or $t = 0.40$) coincide with cell midpoints.

Two computations were performed in each case, using the Godunov method and the GRP scheme, respectively. In the shock test case (Figure 2(a)) both methods agree quite well with the exact solution. However, taking a closer look at the results, the GRP solution is in better agreement with the step function in the two cells immediately adjacent to the shock front. This demonstrates the "high-resolution" capability of GRP. We remark that here a sharper "shock capturing" is obtained by a second-order extension of the (first-order accurate) Godunov method, even though the monotonicity constraint imposed on the GRP solution effectively reduces the scheme to first-order accuracy near discontinuities (by imposing a near-zero slope at cells adjacent to the jump).

The second test case (Figure 2(b)) was devised to demonstrate the relative performance of the two schemes in a setup leading to shock formation from an initially continuous data. Here the gap between the results produced by the two schemes is considerably wider. In

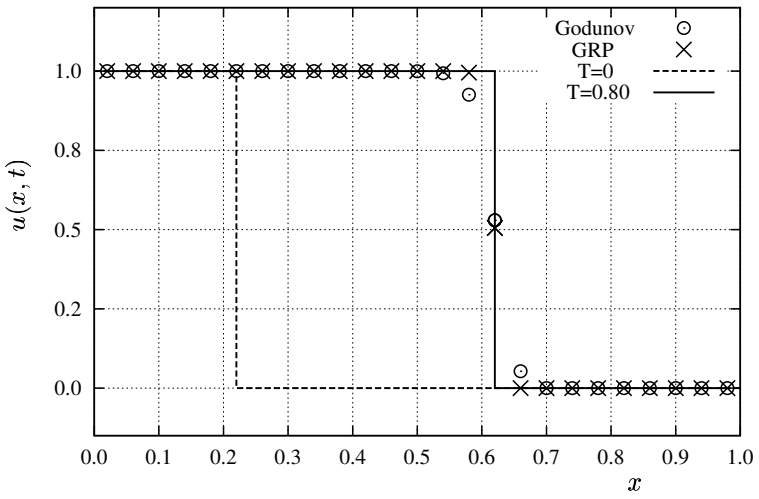

(a) Shock propagation from an initial step function

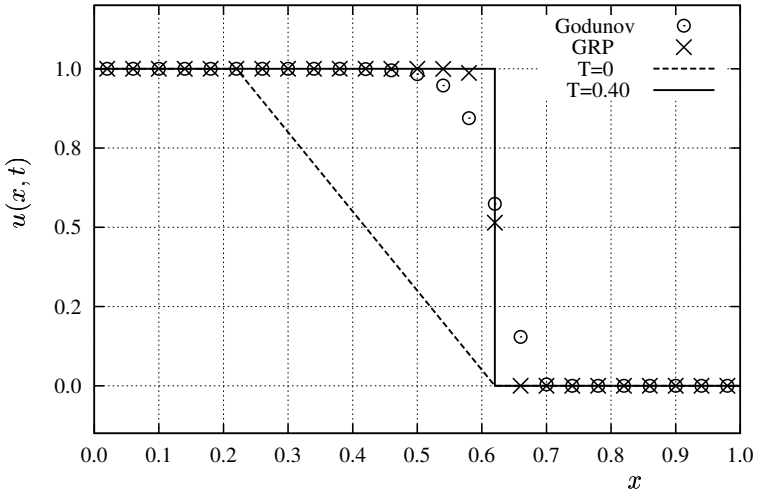

(b) Shock formation from an initial ramp function

Figure 2. The Burgers equation $u_t + (u^2/2)_x = 0$: Shock formation and propagation.

the two or three cells on either side of the jump the GRP solution is in far better agreement with the step function than the Godunov solution. This indicates that when smooth data is considered, the improved accuracy achieved by the second-order-extended GRP method is even higher than the respective improvement in the case of discontinuous data.

Having demonstrated the validity of Godunov/GRP schemes in one space dimension, we turn to the more elaborate case of a two-dimensional scalar conservation law. Our sample problem is due to Guckenheimer (1975) who analyzed the equation

$$\frac{\partial}{\partial t}u + \frac{\partial}{\partial x}(u^2/2) + \frac{\partial}{\partial y}(u^3/3) = 0, \tag{11}$$

with the Riemann-like (constant values in sectors of the plane) data

$$u(x,y,0) = u_0(\theta) = \begin{cases} 0 & \text{in sector} \quad 0 < \theta < \frac{3\pi}{4}, \\ 1 & \text{in sector} \quad \frac{3\pi}{4} < \theta < \frac{3\pi}{2}, \\ -1 & \text{in sector} \quad \frac{3\pi}{2} < \theta < 2\pi, \end{cases} \tag{12}$$

where $\theta = \arctan(\frac{y}{x})$ (see also Figure 3(a)). For this case the exact (self-similar in $\xi = x/t$, $\eta = y/t$) solution was found by Guckenheimer and is represented graphically by the $u =$ *constant* map in Figure 3(b) (along with shock fronts). The numerical solutions obtained by the Godunov and GRP methods (using Strang-type splitting) are shown in Figure 4, with a comparison to the exact solution (the circles mark the characteristic lines denoted by $L = 9, ..., 13$ in the centered wave of Figure 3(b), beginning with the sonic shock). Clearly the GRP solution is more accurate than the Godunov solution in the centered wave region where the solution varies smoothly. We refer to Ben-Artzi and Falcovitz (2003), Chapter 3, for a more detailed account of this sample problem.

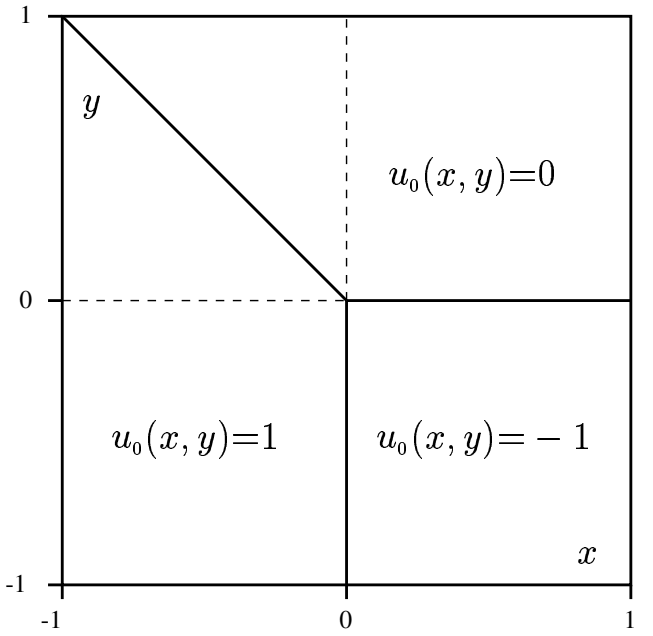

(a) Initial data for Guckenheimer Structure

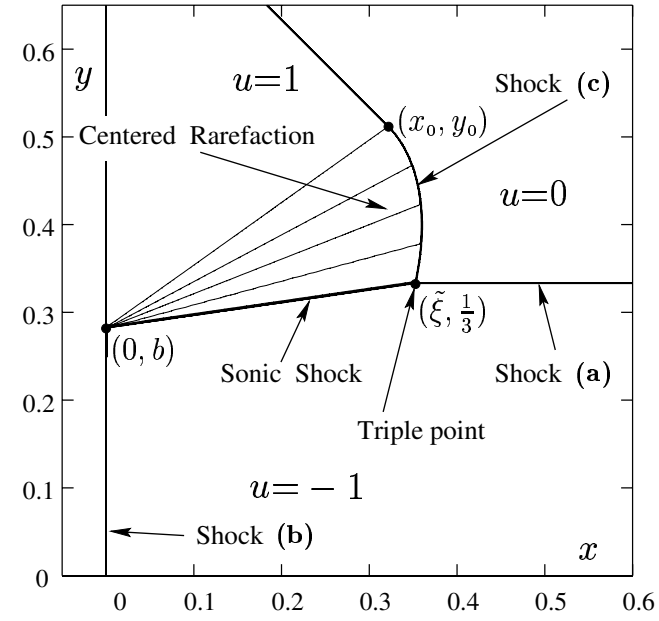

(b) Exact Guckenheimer Structure at t=1

Figure 3. The Guckenheimer Structure for $u_t + (u^2/2)_x + (u^3/3)_y = 0$.

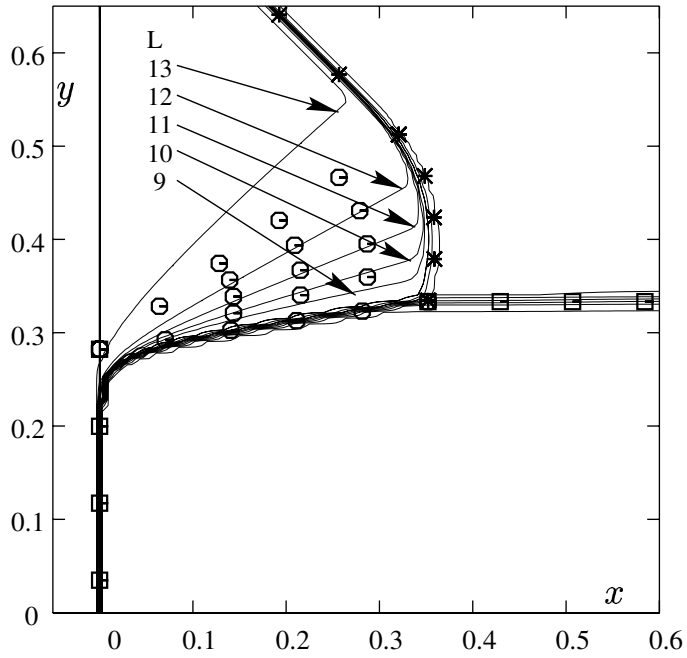

(a) First-order (Godunov $\Delta x=\Delta y=0.00625$)

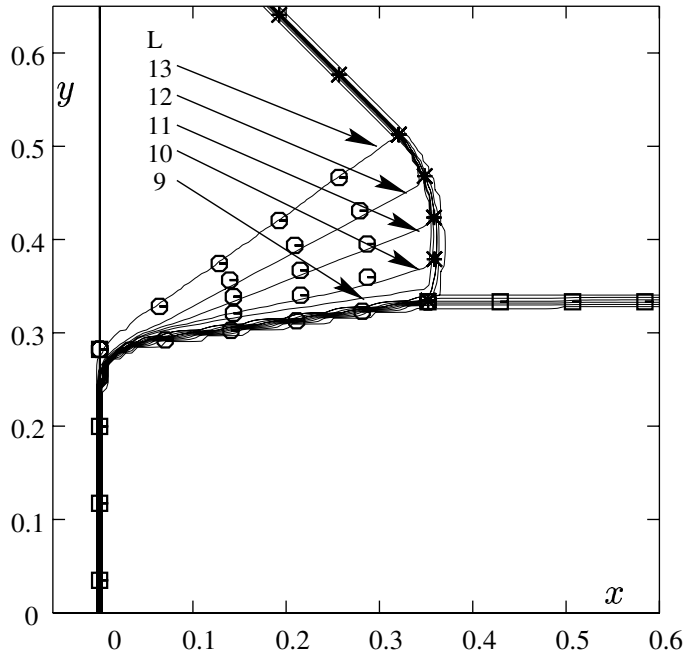

(b) Second-order (GRP $\Delta x=\Delta y=0.00625$)

Legend

- curved or oblique shock
- planar shock (x-facing or y-facing)
- characteristic lines (or sonic shock)

Figure 4. U-level curves for Guckenheimer equation at $t=1$
$u_t + (u^2/2)_x + (u^3/3)_y = 0$. Initial data in Figure 3(a).

The significance of this test case is that it validates the Godunov/GRP schemes in a setup of genuinely two-dimensional wave interaction. In particular (referring to the discussion in the introduction), this result serves to demonstrate the validity of constructing two-dimensional numerical solutions using a one-dimensional scheme with Strang-type operator splitting.

4. Second reflection of a shock wave by a double wedge

Here we consider the reflection of a shock wave from a double wedge. The shock is regularly reflected from the first wedge, and the incident/reflected shock pattern is subsequently reflected from the second wedge. In our case the surface of the second wedge is parallel to the incident shock front, as shown in Figure 5(a). The case considered here is an incident

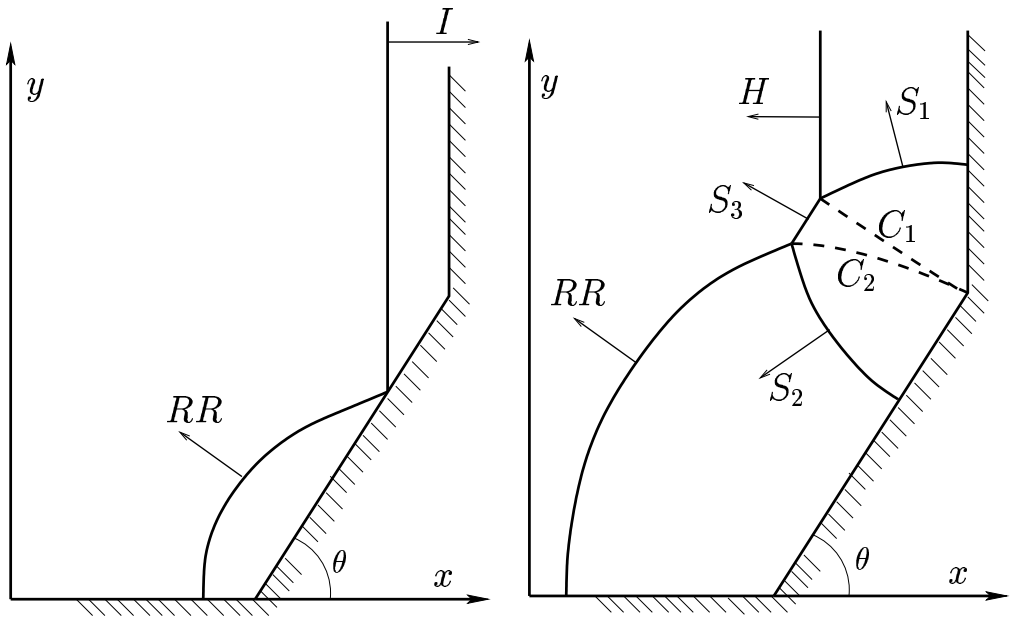

(a) First (regular) reflection (b) Second reflection

Figure 5. First (regular) and second shock reflection from a double wedge.

shock propagating into still air at a Mach number $M_i = 1.488$. The wedge angle is $\theta = 55°$. For a more detailed account of this study, as well as additional cases of shock Mach number and wedge angle, we refer to Falcovitz et al. (1993).

Since the incident shock I is regularly reflected (curved shock RR) by the wedge surface, the flow is self-similar in some finite region about the point of reflection. In this region the reflected shock is planar. Therefore the second reflection is also self-similar in some finite region about the second corner. Based on experimental visualization and numerical simulation, the wave pattern following the second reflection may be schematically depicted as in Figure 5(b). The incident shock I was reflected head-on from the second wedge producing

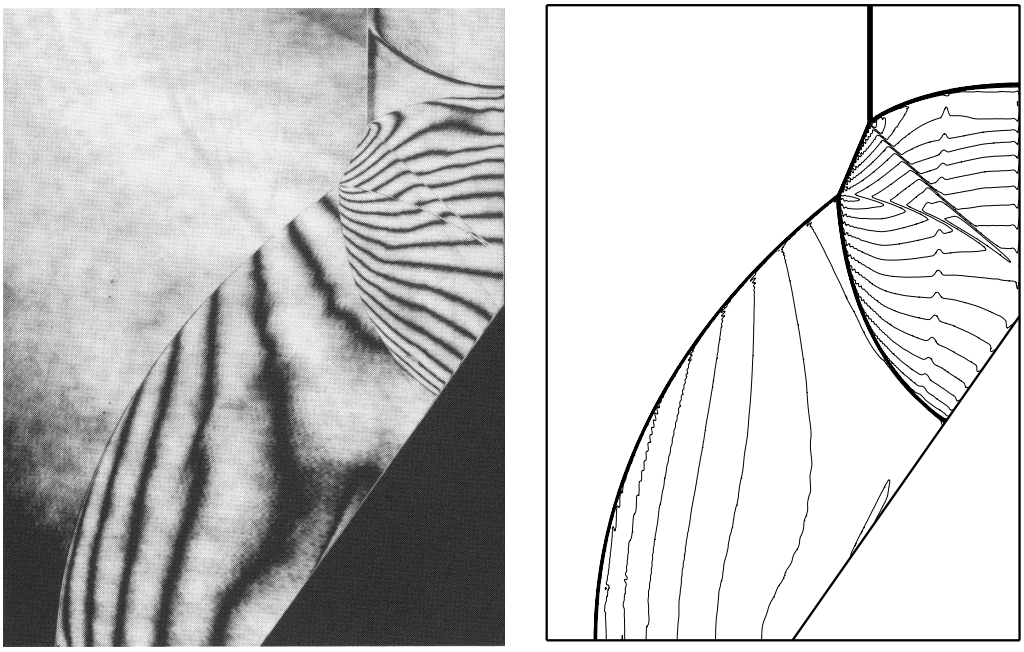

(a) Experimental (b) Computation

Figure 6. Second reflection of $M_s = 1.488$ shock with a double wedge at time $t = 206$.

a planar shock H. Two curved shocks S_1 and S_2 propagate away from the wedge corner. Their interaction with H and with RR, respectively, produces a common "Mach stem" S_3 and two contact (slip) surfaces C_1, C_2 issuing from the respective triple points. For a finite duration this wave pattern is self-similar.

The experimental and computed flow fields are shown as isopycnics (lines of constant density) in Figure 6, at a time where the pattern due to the second reflection is still self-similar. The computation domain was the rectangle $[0 < x < 105] \times [0 < y < 141]$ (dimensions in mm), which was divided into 525×705 square cells. The wedge started at the point $(x, y) = (54.6, 0)$, and it was inclined to the x-axis by an angle $\theta = 55°$. The computation was performed by the Moving Boundary Tracking (MBT) method (Chapter 8 in Ben-Artzi and Falcovitz, 2003) where the wedge served as a stationary rigid-wall boundary. A rigid-wall boundary condition was also imposed at all other boundaries of the computation domain, except the edge $x = 0$ where an inflow boundary condition corresponding to the incident shock was imposed. The initial position of the shock was $x = 53.6$, and the fluid state ahead of the shock was $[\rho, p, u]_o = [1.20, 0.0985, 0]$ (in mks units). The fluid was taken as an ideal gas with $\gamma = 1.4$. The integration time step was calculated at each cycle so as to have a CFL ratio of $\mu_{CFL} = 0.7$.

Consider the experimental isopycnics given in Figure 6(a) and the corresponding computational map in Figure 6(b). The incident shock has already been reflected from the second wedge (which is simply the shock tube endwall), and is clearly visible as a planar shock segment parallel to the endwall. The regularly-reflected curved shock is also visible; it is joined to the latter by a short (oblique) shock segment, whose endpoints are the previously

mentioned "triple points", just as in a classical Mach reflection. Each triple point marks the intersection of three shocks and a slip surface, all clearly visible on both the experimental and computational maps. The two curved shock are produced by the "secondary" reflection at the wedge corner, which commences upon the arrival of the regular reflection point at that corner (the curved shock issuing from the upper right corner in the experiment is due to leakage and should be disregarded).

The agreement between the experimental and computed wave fronts and isopycnic lines is very good. The fact that this complex shock pattern was well reproduced by the GRP/MBT scheme constitutes a validation of the scheme for two-dimensional shock interaction phenomena.

5. Drag by shock interaction with a suspended body of revolution

5.1 Drag on a sphere

The interaction of a planar shock wave with a sphere results in a reflected shock that eventually evolves into a Mach reflection pattern that diffracts around the sphere converging toward the axis of symmetry. The time-dependent pressure distribution on the spherical surface produces a dynamic drag force that peaks before the shock front traverses the spherical midplane, then gradually evolves toward the steady state value corresponding to the post-shock flow. The drag coefficient (related to the post-shock flow) reaches a peak value much higher that the respective steady value.

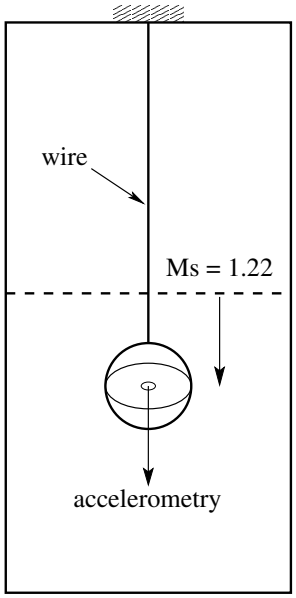

Figure 7. Suspended sphere in a vertical shock tube.

This physical situation was recently studied for a sphere suspended in a vertical shock tube (Tanno et al. 2003), by double-exposure holographic interferograms and by accelero-

metric measurement of the drag force history. The experimental setup is shown schematically in Figure 7. For the simulation of the shock-sphere interaction (using GRP/MBT) the computation was conducted in a rectangular domain of dimensions $x \times y = 300 \times 150$ [mm], with a grid of 0.25×0.25 [mm] square cells (the half-circle represents the sphere, and $y = 0$ is the axis of symmetry). In a sample isobar map at time $t = 60\,[\mu s]$ (see Figure 8) we observe a Mach reflection with a small Mach stem. As the drag coefficient history in Figure 9 shows, the drag force has reached its peak value at approximately that time.

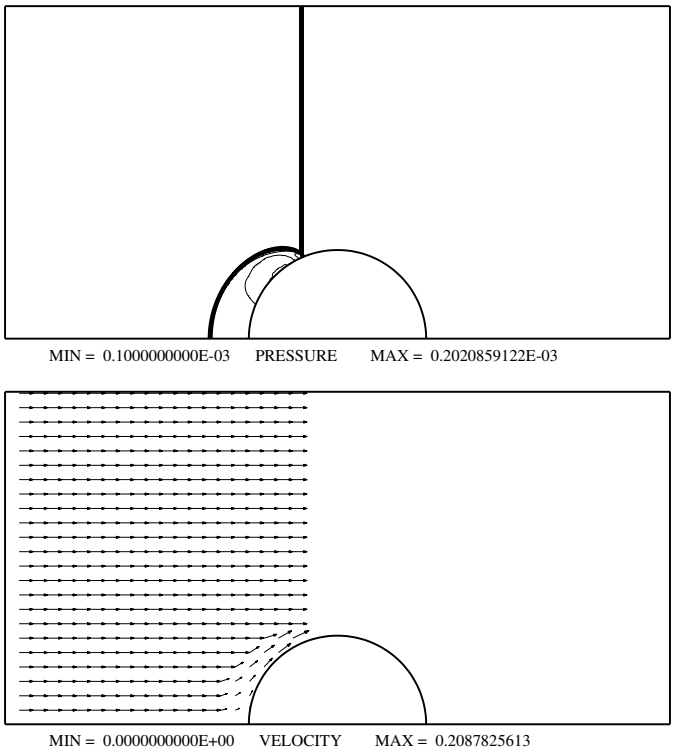

Figure 8. Isobars for sphere interaction with $M_s = 1.22$ shock wave ($t = 60$).

Evidently, elimination of high-frequency fluctuations of the measured data (by suitable smoothing) would greatly improve the agreement with the computed drag history (Figure 9). This novel and useful application of accelerometry to dynamic drag measurement will probably be further refined in the future.

5.2 Drag on a cone

The interaction of a planar shock wave with a cone suspended from its apex (K. Tamai 2004) can produce a regular reflection, or a Mach reflection as shown in Figure 10 for the case of an $M_s = 1.23$ air shock and cone angle of 40°. Assuming uniform conditions behind the incident shock, the flow about the cone is self-similar with respect to the time if $t = 0$ is taken as the shock arrival time at the cone apex. Consequently, the drag force must be

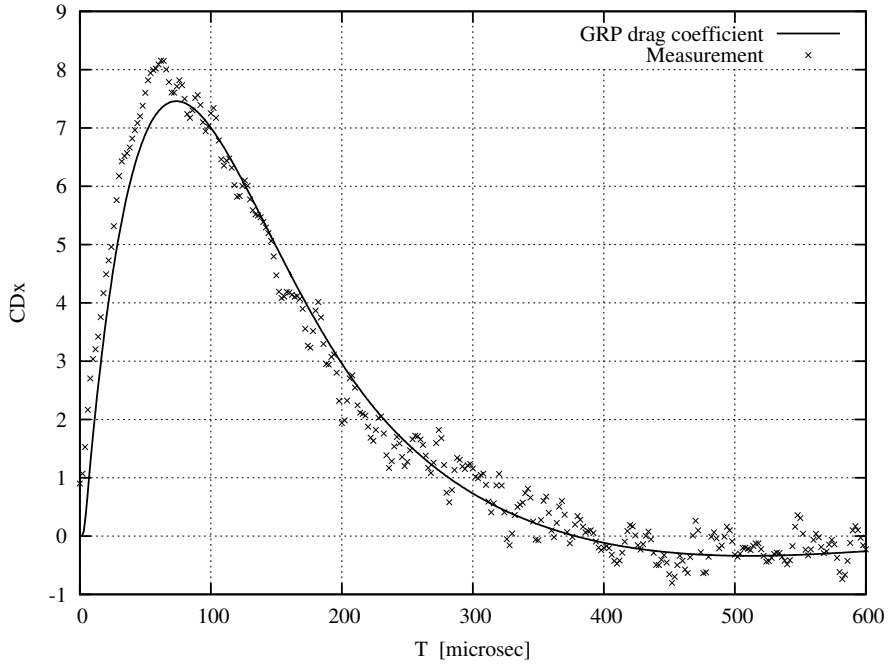

Figure 9. Drag coefficient history ($M_s = 1.22$ shock wave).

proportional to t^2.

For the (GRP/MBT) simulation of the shock-cone interaction we used a rectangular domain of dimensions $x \times y = 400 \times 150$ [mm] ($y = 0$ is the axis of symmetry), with a grid of 0.5×0.5 [mm] square cells. The isobar map at time $t = 240\,[\mu s]$ (Figure 10) clearly shows a Mach reflection pattern, which is understandable considering the relatively small half-cone angle of 20°.

In the drag coefficient history (Figure 11(a)) the drag force reaches its peak value at the moment that the shock diffracts around the cone base (about $t = 260$). That time also marks the end of the previously mentioned self-similar flow pattern. In order to bring out that similarity, we show in Figure 11(b) the variation of the square root of the force $F_x^{1/2}$ with time, which in theory should be a linear function. The computation result is clearly in excellent agreement with that theoretical condition. However, the measurement displays some unexplained monotonically increasing pattern that "crosses over" at about $t = 100\,\mu s$ from an overvalued force to an undervalued force. This result seems to indicate that the method of measurement, including its dynamic hammer calibration, requires careful review. We may expect that further improvements and refinements will result in more accurate accelerometric force measurement.

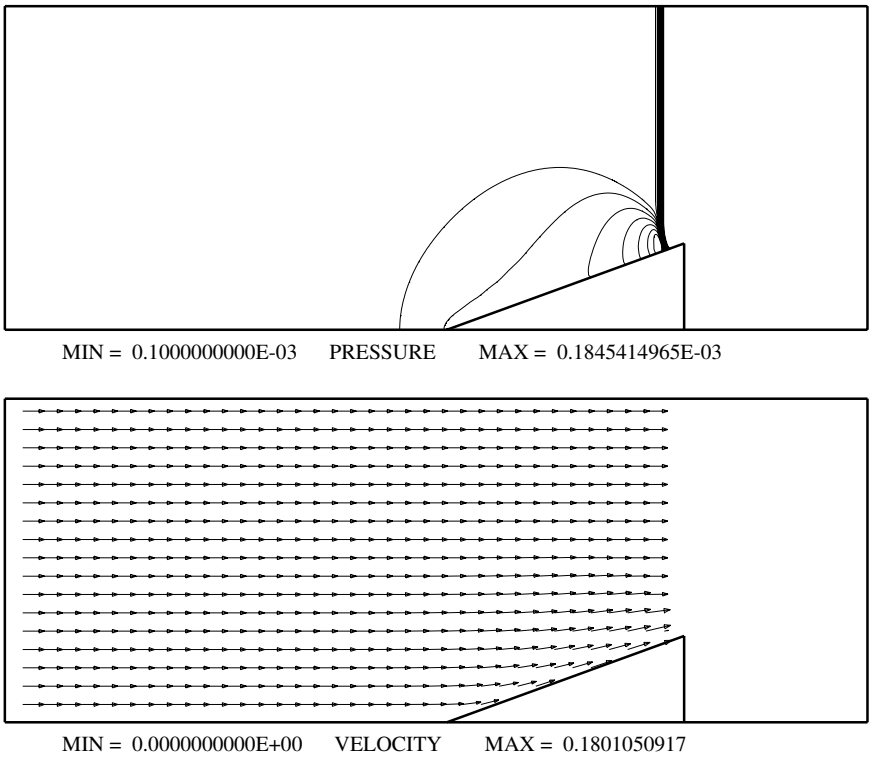

Figure 10. Isobars for cone interaction with $M_s = 1.23$ shock wave ($t = 240$).

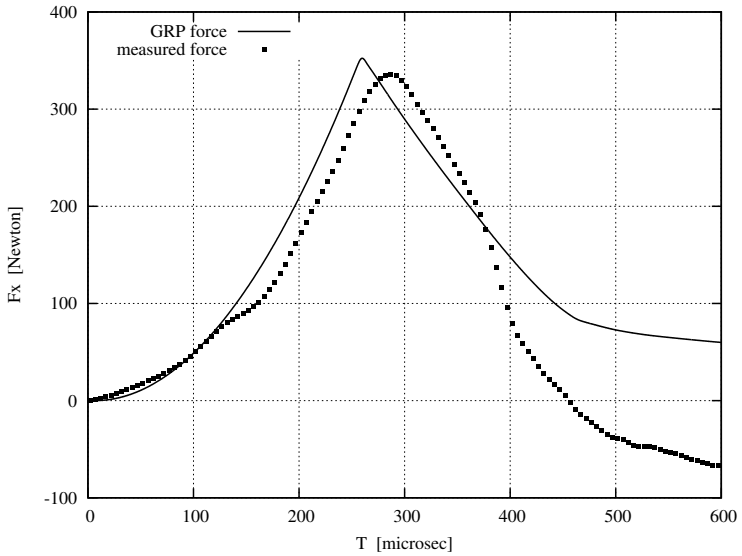

(a) Drag force F_x as function of time

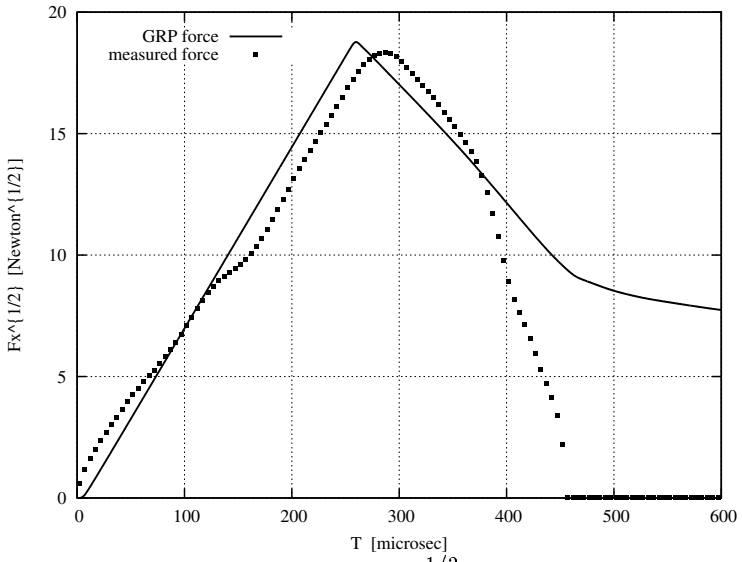

(b) Square root of drag force $F_x^{1/2}$ as function of time

Figure 11. Drag force on a 40° cone due to $M_s = 1.23$ shock in air.

6. Summary and conclusions

The GRP scheme for hyperbolic conservation laws has been introduced in the simpler context of scalar equations. It has been demonstrated that this method produces high-resolution results for 1-D and 2-D shock interactions in the scalar case. This is taken as a validation of the operator splitting by which a 2-D (or even 3-D) finite-difference approximation may be constructed using only a 1-D "GRP solver".

Our main fluid dynamical validation study was a shock interaction problem where a second reflection from a double wedge produced a (nearly) self-similar pattern of "corner-reflected" waves. A good agreement was obtained between experimental flow visualization and GRP computations, supporting the scheme validation in this case of complex shock interaction.

Using a recently developed technique of accelerometric drag measurement, we considered the cases of a sphere or a cone suspended in a vertical shock tube. This innovative method enables the measurement of dynamic drag forces due to shock loading. The GRP simulations helped in pointing out that (especially in the case of the cone, where similarity arguments supported the validity of the computed drag history), the accelerometric method requires further refinement.

References

Ben-Artzi M, Falcovitz J (2003) *Generalized Riemann problems in computational fluid dynamics*. Cambridge University Press, London

Falcovitz J, Alfandary G, Ben-Dor G (1993) Numerical simulation of the head-on reflection of a regular reflection,
International Journal for Numerical Methods in Fluids, 17:1055–1077

Godunov S K (1959) A finite difference method for the numerical computation of discontinuous solutions of the equations of fluid dynamics, Mat. Sbornik **47**:271–306

Guckenheimer J (1975) Shocks and rarefactions in two space dimensions, Arch. Rational Mech. Anal., 59:281–291

von Neumann J (1943) Oblique reflection of shock waves. Explosive Research Report No 12, Navy Department, Bureau of Ordnance, Washington DC. (Reprinted in: Collected Works of J. von Neumann, Pergamon Press, 1963, 6:238–299)

Minota T (1993) Interaction of a shock wave with a high-speed vortex ring, Fluid Dyn Res 12:335–349

Tamai K (2004) Shock dynamics study of development of blast wave loading facility and tempered glass production, Doctor thesis, Interdisciplinary Shock Wave Research Laboratory, Institute of Fluid Science, Tohoku University, Sendai, Japan.

Tanno H, Itoh K, Saito T, Abe A, Takayama K (2003) Interaction of a shock wave with a sphere suspended in a vertical shock tube, Shock Wave Journal 13:191–200